Tidal and wind-driven surface currents in the German Bight: HFR observations versus model simulations

**Alexander Port · Klaus-Werner Gurgel · Joanna Staneva ·
Johannes Schulz-Stellenfleth · Emil V. Stanev**

Abstract Tidal and wind-driven surface currents in the German Bight between shallow mudflats of the North Frisian islands and the island of Helgoland are studied using coastal high-frequency radar (HFR) observations and hindcasts from a primitive equation numerical model. The setup of the observational system is described, and estimates of expected measurement errors are given. A quantitative comparison of numerical model results and observations is performed. The dominant tidal components are extracted from the two data sources using tidal harmonic analysis and the corresponding tidal ellipses are defined. Results show that the spatial patterns of different tidal ellipse parameters are consistent in the two data sets. Model sensitivity studies with constant and variable salinity and temperature distributions are used to study density-related mechanisms of circulation. Furthermore, the role of the surface wind field in driving the German Bight circulation is investigated using the complex correlation between wind and surface current vectors. The observed change of the respective correlation patterns from the coastal to open ocean is shown to be due to a combination of density effects, the coastline and topography. The overall conclusion is that HFR observations resolve the small-scale and rapidly evolving characteristics of coastal currents well in the studied area and could present an important component for regional operational oceanography when combined with numerical modelling. Some unresolved issues associated with the complex circulation and large instability of circulation in front of the Elbe River Estuary justify further considerations of this area using dedicated surveys and modelling efforts.

A. Port (✉)
ICBM, University of Oldenburg, Oldenburg, Germany
e-mail: alex.port@gmx.com

K.-W. Gurgel
Institute of Oceanography, University of Hamburg,
Bundesstrasse 53, 20146 Hamburg, Germany
e-mail: gurgel@ifm.uni-hamburg.de

J. Staneva · J. Schulz-Stellenfleth · E. V. Stanev
Institute for Coastal Research, GKSS Research Centre,
Geesthacht, Germany

Present Address:
A. Port
Department of Earth and Ocean Sciences,
University of Waikato,
Hamilton, New Zealand

1 Introduction

High frequency (HF) radars operate in the decametre range of radio frequencies and provide remotely sensed area-covering data sets of surface currents. Depending on the operating frequency, the measurements can reach ranges of up to 200 km along the ocean surface, covering thousands of square kilometres. In contrast to satellites, which pass a location every couple of days, an HF radar can observe an area of interest continuously at sampling rates of as little as a few minutes.

Currently, ocean observing systems, some of them including HF radars, are installed along selected coastal areas worldwide, implementing an approach which combines measurements and models by data assimilation (Breivik and Sætra 2001; Paduan and Shulman 2004; Shulman and Paduan 2009; Hoteit et al. 2009; Barth et al. 2008, 2010, 2011). Before combining measurements and models, investigations on data quality and model statistics are necessary to check if the measurement errors are small enough to support the model and if major processes found in the measurements have been well captured by the model.

Model errors can have many sources, for example, the missing implementation of certain physical processes, a poor spatial or temporal resolution or errors in the forcing fields. Quantification of these different contributions is not trivial. Likewise the estimation of observation errors is a demanding task, and, as demonstrated here, particularly in the case of remote sensing systems like HF radar. These systems are characterised by a complex imaging process, which is influenced by many different parameters. Although the study presented here does not deal with data assimilation, the analysis of inconsistencies between observations and simulations is a first step in this direction. Thus, the issue of inconsistency is considered here as an inherent property of observational systems and numerical models. This approach not only identifies the geophysical relevance of observations and results from simulations but also addresses the limits of observational and prediction systems. This could contribute to improving estimates of the state of the coastal ocean, which is the general objective motivating our present research.

The region of interest in this study is the German Bight, situated in the Southern North Sea (Fig. 1) and bounded by the Netherlands and Germany to the south as well as Denmark and Germany to the east. This is a shallow coastal area with a rectangular geometry, limited by the zonal direction of the coastline towards the Netherlands and the meridional direction towards Denmark. An extension of the Elbe Estuary towards the northwest can be seen in the bathymetry.

Ocean processes in the German Bight are mostly driven by tides, as a result a Kelvin wave propagates eastwards along the southern coast and northwards along the eastern coast of the Bay. The sense of rotation of tidal ellipses is principally determined by the relative strength of Coriolis force, sea-surface pressure gradients and friction. Taylor's theoretical calculations for a rectangular basin (Taylor 1922) suggest positive ellipticity (anticlockwise rotation) in the German Bight. However, large-scale coastal geometry is not the only
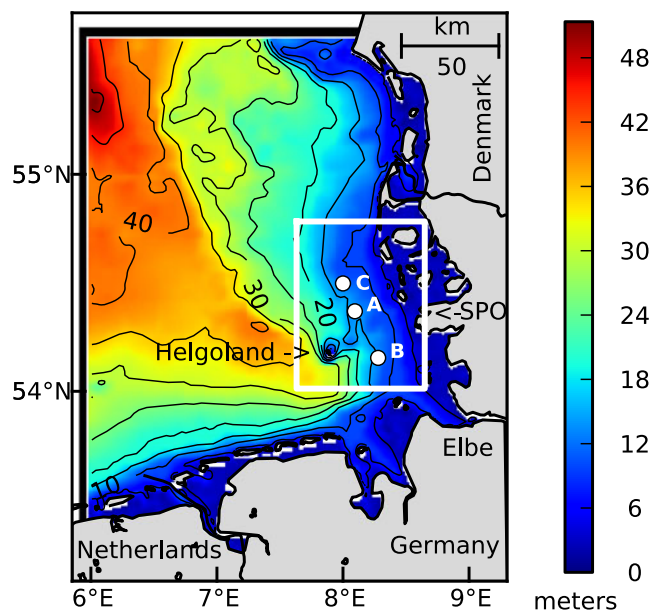

Fig. 1 The region of interest as defined by the hydrodynamical model domain covers the German Bight, with open boundaries to the north and west (*thick black lines*). Bathymetry as used in the model setup is shown in metres, color-coded according to the *colorbar*. The *rectangular white inset* outlines the HFR observation grid domain. The island of Helgoland is visible in the southwestern corner of this inset, as well as the relatively shallow area east–northeast of it, which is also known as Steingrund. At the eastern edge of the observation grid lies St. Peter-Ording (*SPO*). The Elbe Estuary enters the German Bight from the southeast. Locations *A* and *B* (*white circles*) indicate grid points from which time series are presented in Fig. 10. The two locations were chosen as a compromise between high coverage over time (see Fig. 2) and low GDOP (see Fig. 3), one north and one south of the baseline connecting the two HFR systems (see also Fig. 2). Time series for 10 m wind from the ECMWF reanalyses in location *C* were used for complex correlation analysis (see further in text)

source of ellipticity. Bathymetric gradients, which are not accounted for in Taylor's theory, also cause ellipticity changes. Furthermore, the shallow German Bight is a transition area where geophysical balances change from geostrophy to friction domination, with accompanying changes to the rotation.

Most of the freshwater input for the German Bight ($\approx 1,000$ m^3 s^{-1}), mainly from the rivers Elbe and Weser, is in the southeastern corner of the Bight, making dynamics there extremely complex. It is therefore expected that the influence of geometry (including topography) and stratification (dominated by inputs of freshwater) will control the local dynamics there. Internal friction could also play an important role, for example Carbajal and Pohlmann (2004) show that baroclinic effects significantly modify the inclination of tidal ellipses.

The German Bight has been characterised in numerous studies dealing with observations and numerical
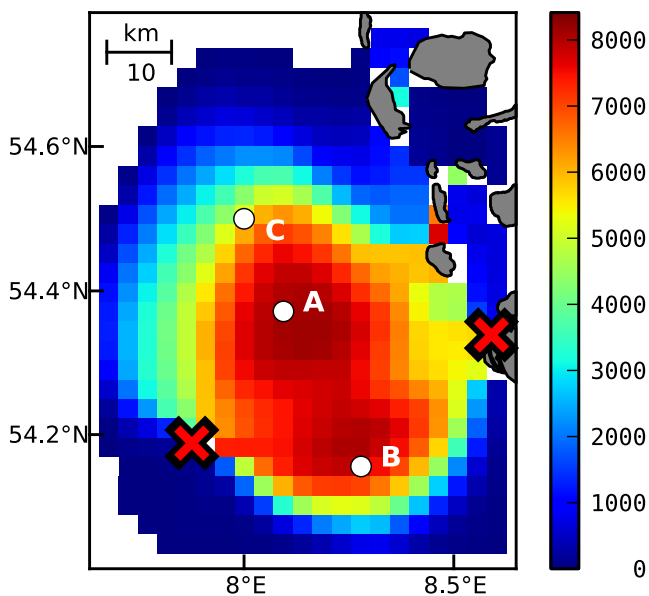
Fig. 2 Temporal coverage of the HFR surface velocity observations: the number of samples available at each grid point is color-coded according to the *colorbar*. The entire dataset (6 months) comprises 8,414 samples in time. The data collected during September 1991 was extracted for further analyses. Islands in the northeast and east as well as the mainland coast in the east are shown in *gray*, the HFR system locations are indicated by *red-on-black crosses*: the western location on the island of Helgoland (occluded at this scale) and the eastern location near the village of St. Peter-Ording. Locations *A*, *B* and *C* are reproduced from Fig. 1

characteristics in the German Bight, *but now providing more focus on errors and inconsistencies between observations and numerical simulations.* Here we will use different observational data sets and numerical model setups. We demonstrate that the analysed historic data set is well suited for the investigation of novel features in the dynamical control mechanisms. Our work also incorporates outputs from finer resolution numerical models with up-to-date physical parameterizations not used in previous studies. First activities to use such models for pre-operational assimilation of HFR data in the German Bight exist and an assessment of their performance, e.g. regarding spectral characteristics of dominating signals, is therefore of utmost importance.

The *first objective* of this paper is to analyse a data set of surface currents acquired by HF radar in the German Bight from 9 August 1991 to 4 February 1992 with the aim of deriving a geophysically relevant information on dominating processes. This analysis is preceded by a detailed description of the observational setup and quantification of the expected measurement errors.

The *second objective* is to critically compare surface currents from radar observations with the ones simulated by a state-of-the-art numerical hydrodynamical model (General Estuarine Transport Model, GETM; Burchard and Bolding 2002). This enables to (1) validate the quality of simulations and (2) use validated

modelling. Two of them, Schirmer et al. (1994) and Carbajal and Pohlmann (2004), could be considered as precursors of the present paper. The former study estimated tidal ellipses for different tidal constituents from "Coastal Ocean Dynamics Applications Radar" (CODAR; Barrick et al. 1977) measurements carried out in the German Bight showing clearly that the input of freshwater and, in general, baroclinic effects favored clockwise rotation in this region. The major changes occurred in the neighbourhood of the openings of the embayments. According to Carbajal and Pohlmann (2004), stratification produces negative ellipticity almost everywhere in the German Bight.
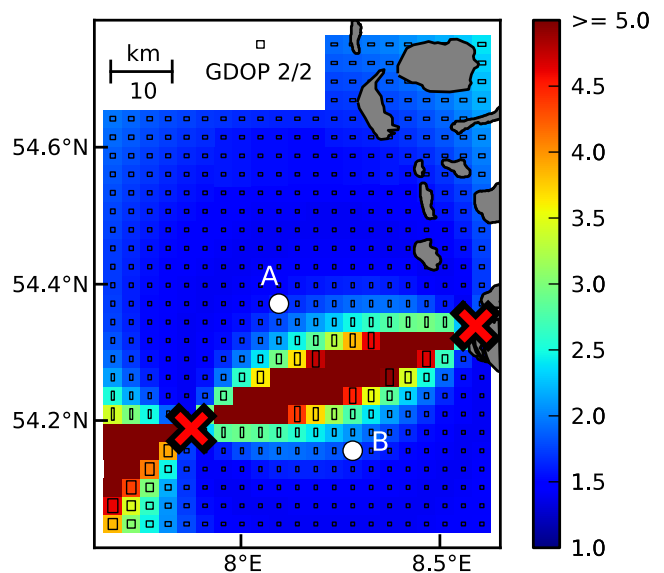
According to Soulsby (1983), the boundary between the clockwise and anti-clockwise component of the flow could be, in some cases, a good indication of thermal fronts. In the case of the German Bight, the haline front is more important (Czitrom et al. 1988), in particular in the southeastern corner, which is the major area of our interest.

One specific motivation for the present study is to revisit analyses of observations and numerical modelling presented by Schirmer et al. (1994) and Carbajal and Pohlmann (2004) of the spatial dependence of tidal

Fig. 3 Spatial distribution of the observation error due to geometry. The boxes' height and width indicate the north and east components of GDOP, with a fictitious box for a GDOP value of 2 for both components displayed at the *top* of the map as scale. The *color scale* gives the absolute value. Locations of *A* and *B* are as in Fig. 1

simulations to gain insight into geophysical processes, e.g. based on sensitivity experiments.

The regional impact of individual forcing factors, in particular wind forcing, has not been enough considered in the earlier studies. This is an important point for the present study because the main source of data, which is the HFR, provides information only about sea surface currents, which are strongly affected by wind. At the same time, the shape of the coastline as well as the bottom topography have a big impact on the wind-driven circulation in general.

It is also known that even in a continental shelf where the bathymetry is relatively simple (e.g. West Florida Shelf), the subtidal surface current patterns could be very complicated in response to local wind, in particular close to the coast (Liu et al. 2007). One could thus expect that the correlation between wind and surface current in the coastal area of German Bight will be much more complex than in the open sea. Quantifying dominating forcing and response effects is the *third objective* of the present study.

The paper is structured as follows: In Section 2, we overview the available data from observations and numerical simulations, as well as methods used to analyse them. Preparatory analysis of simulated circulation patterns in the German Bight is presented in Section 3. Section 4 deals with model data intercomparison, followed by a general discussion of results and conclusions.

2 Data sources and analysis methods

2.1 HFR observations

Within a German national research project ("PRISMA", BMFT-Projekt 03F0558A1; PRISMA 1994), the University of Hamburg had installed two HFRs, one on the mainland coast near the village of St. Peter-Ording at 54.34° N, 8.59° E and one on the island Helgoland at 54.19° N, 7.88° E, about 50 km offshore in the German Bight. The region of interest surrounding the area covered by these two HFRs coincides with the domain of the numerical model described in Section 2.2 and is shown in Fig. 1, with the bathymetry information as used in the hydrodynamical model setup. Figure 2 shows in more detail the locations and the area covered by both HFRs. The achieved range of the radar system is typical for the operating frequency used. The HFRs used within "PRISMA" were based on an early CODAR design developed at NOAA (Barrick et al. 1977) and had been modified at the University of Hamburg. In contrast to more recent systems, like the

CODAR SeaSonde (Lipa et al. 2006) and the WERA system (Gurgel et al. 1999a, b), these systems transmitted pulses of electromagnetic waves for range resolution and four receive antennas arranged in a square for finding the azimuth of the echoes. Modifications had been made to filters, amplification and mixing components, as well as the digital control circuits in order to reduce internal system noise and increase the dynamic range.

The systems were operated from August of 1991 until February of 1992 to measure surface current velocities. Both HFRs were operated at 29.85 MHz, measuring the radial component of the surface current averaged over a layer extending to approximately 0.5 m below the sea surface. A lower radar frequency would result in an extended range; however, due to the water depth in the German Bight, frequencies as low as 5 MHz should not be used because the Bragg-resonant ocean waves show a very low wave height, or do not exist at all (cf. Liu et al. 2010).

To map the radial components onto a cartesian grid with 3 km resolution, all radial components within a circle of 3 km radius around a cartesian grid point were selected and processed to calculate average and standard deviation. These values were then used to compute the estimates of zonal and meridional surface velocity together with the corresponding observation error estimates. Details of this algorithm can be found in Barth et al. (2010). Every 30 min, data collected over 18 min of "coherent integration time" (CIT) was processed to produce one sample at a time.

The observation error estimate consists of two major components: The error of the radial surface current, which is calculated as described in Barth et al. (2010) and includes current variability within the CIT, and a factor describing the influence due to geometry called "geometric dilution of precision" (GDOP; Chapman et al. 1997). The GDOP is well-known from the satellite-based "global positioning system" and has exactly the same meaning in this context.

The spatial distribution of the GDOP for the HFR measurement grid (Fig. 3) proves that around the line connecting the two HFRs, high errors related to geometry can be observed (GDOP ≥ 5) because the angle between the two radial components becomes too large. Instead of removing the data at these grid points, an interpolation technique has been applied: In a first step, all grid points with GDOP < 5 are processed by combining the radial components. In this way, the 2D current field is calculated everywhere except around the connection line. In a second step, the components perpendicular to the connection line are interpolated from the surrounding 2D current field at the grid points

omitted in the first step. These interpolated values are then combined with a measured radial component from the radar site providing the smaller error. A similar approach was used to compute the observation error estimates.

The mean observation error over 6 months (Fig. 4) is calculated from the error of the radial components, or in case of GDOP $\geq$ 5 estimated using the interpolation procedure described above. As a result, the errors around the baseline connecting the two HFR system locations are much smaller than the GDOP values given in Fig. 3 suggest. Without the interpolation, the high GDOP values around the connection line may have resulted in errors of 1 m/s or more. Some influence of the geometry on the measurement error can still be seen in the meridional component.

The errors of the HF radar-measured near-surface currents discussed in this paper have been derived from the statistics of the measurements (cf. Barth et al. 2010). There are also several papers which discuss comparisons of currents measured by HF radars and in situ observations. These comparisons mostly report the root mean square (RMS) differences between the two measurements, which could not be divided into the errors of each of the instruments separately. Additional problems arise because area-averaged data are compared to point measurements and near-surface measured data are compared to measurements at some depth below the surface, which may result in high RMS differences in case of horizontal or vertical current shear. The differences reported in the literature range from 11–20 cm/s for an Ocean Surface Current Radar (OSCR) type system off the Coast of North Carolina, USA (cf. Graber et al. 1997) to 10–20 cm/s for the modified CODAR used in this paper (cf. Essen et al. 2000). More recent papers discuss RMS differences observed

with WERA measurements under conditions of high current velocities up to 180 cm/s associated with a large current shear within the East Florida Current (cf. Parks et al. 2009), where comparisons to ADCP measurements at 14 m below the sea surface gave an RMS difference of 10–30 cm/s, which corresponds to 5.5–17% of the measured velocities. Comparisons between ADCP velocities at 4 m below the sea surface and hourly long-range SeaSonde measurements from the West Florida Shelf, which is an area of low current velocities (Liu et al. 2010), resulted in RMS differences of 6–10 cm/s, corresponding to 20–33% of the measured velocity range. HF radar measurements analysed in the present study were not accompanied by ADCP or other in situ observations; therefore, the assumption is made, based on our and other authors results cited above, that the accuracies of the present observational setup are in the range of the previously reported ones.

For purposes of tidal and complex correlation analyses, only those points on the observation grid were included where the coverage over time of the HFR observations is at least 50% and the water depth is at least 5 m (the latter criterion was also applied to model simulation data).

2.2 Numerical simulations

Numerical simulations were performed using the 3D primitive equation GETM (Burchard and Bolding 2002). The nested-grid model consists of a coarse-resolution North Sea–Baltic Sea (3 nautical miles) outer model and a nested German Bight model with a horizontal resolution of about 1 km. Both models have 21 layers in σ-coordinates. The horizontal discretisation is done on a spherical grid. The bathymetric data for both models are prepared using the ETOPO-1 topography, together with observations made available

Fig. 4 HFR observation error estimates are shown separately for the zonal (*left panel*) and meridional (*right panel*) component (color-coded according to the *colorbars*, identical scales). The entire time series consisted of 8,414 samples for observation grid points with full coverage over time
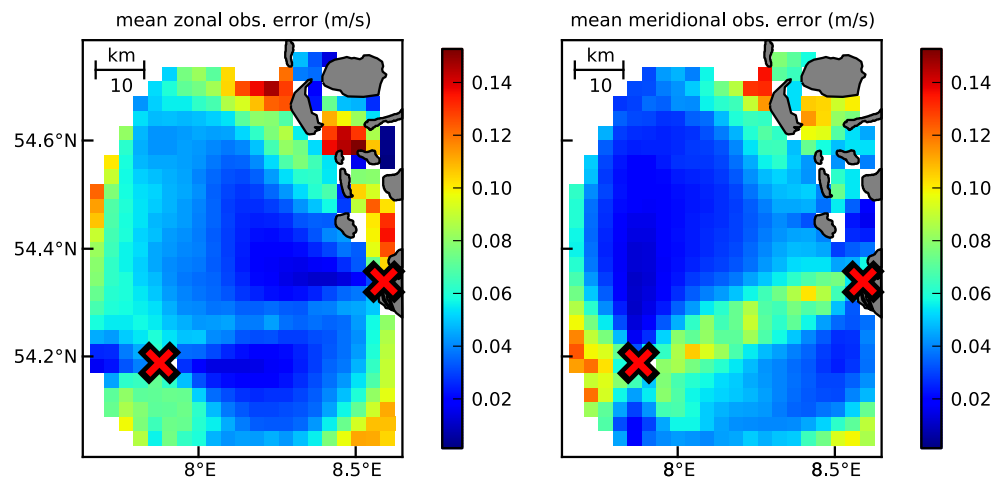
from the German Hydrographic Service (Bundesamt für Seeschifffahrt und Hydrographie, BSH; Dick et al. 2001). The bathymetry as well as the northern and western open boundaries used by the hydrodynamic model are shown in Fig. 1.

The model system is forced by (1) the meteorological forcing derived from bulk formulae using six-hourly reanalysis data, including wind (exemplary wind speed and vector orientation for September 1991 is shown in Fig. 5), mean sea level pressure, air temperature, humidity and cloud cover on a 0.5×0.5° grid from the European Centre for Medium-Range Weather Forecasts (ECMWF); (2) river inflow using climatological data for the 30 most important rivers within the North Sea–Baltic Sea model area provided by the Swedish Meteorological and Hydographical Institute and (3) time-varying lateral boundary conditions of sea surface elevation, temperature and salinity. The sea surface elevation of the western and northern open boundaries of the German Bight setup is taken from the North Sea–Baltic Sea model output with 5 min time interval. The tidal forcing at the open boundaries of the

North Sea–Baltic Sea model towards the Norwegian Sea and the English Channel was constructed from 13 partial tides from the TOPEX-POSEIDON data set. Temperature and salinity at those open boundaries are interpolated at each time step using the monthly mean climatological data of Janssen et al. (1999). The setup has been described in more detail by Staneva et al. (2009).

For comparisons with HFR observations and analyses based on them, currents from the first model σ-level (surface) were bilinearly interpolated to the HFR observation grid. As an example illustrating agreements and disagreements between two data sources, Fig. 6 shows a comparison of surface currents from numerical simulations and HF radar observations for 3 September 1991 at 3:10 UTC and 9:10 UTC. The currents shown in this figure are separated by half the M2 period and illustrate the periodic inflow and outflow of water into the German Bight. It is noteworthy that the HFR coverage can change significantly within one tidal cycle. One can also find a quite heterogeneous behaviour of the deviations between model and measurements.
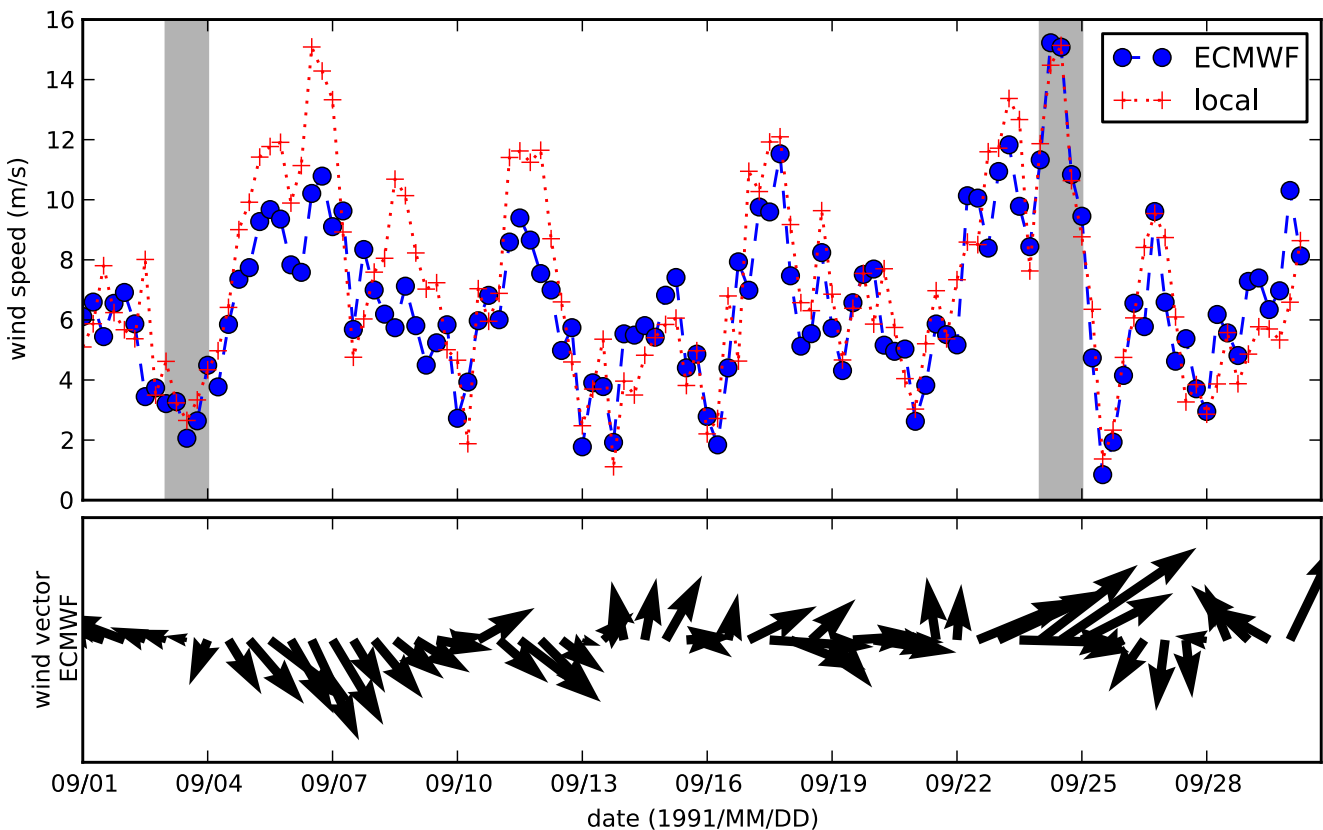
Fig. 5 ECMWF six-hourly reanalysis surface wind speed data as used for model forcing as well as complex correlation analyses. Wind speed and vector orientation (every second data point is plotted for clarity) for September 1991 are shown from the grid point closest to the middle of the HFR observation grid (54.5° N,

8.0° E; see Fig. 2, point C). *Shaded sections* in the *upper panel* show exemplary (relatively) calm (3 September 1991) and stormy (24 September 1991) days as used for surface current time series examples in Fig. 10. For comparison, the *upper panel* also shows data from local observations made in St. Peter-Ording
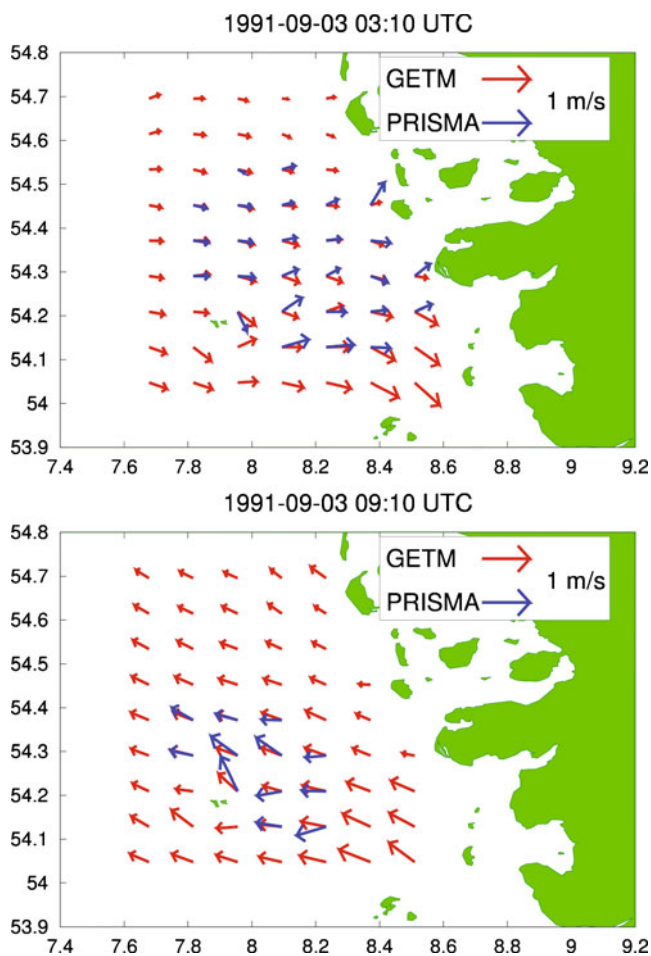
Fig. 6 Surface currents from numerical simulations (*red*) and HFR observations (*blue*) for 3 September 1991 at 3:10 UTC (*top*) and 9:10 UTC (*bottom*)

These issues will be discussed in more detail in the following.

2.3 Tidal analysis

Classical tidal harmonic analysis was performed using the software package t_tide (Pawlowicz et al. 2002). For any type of tidal harmonic analysis, a finite set of tidal constituents must be chosen. Constituents which are unlikely to be resolved for the given length of the time series may be discarded beforehand. A further possibility implemented in t_tide is to refine the set based on signal-to-noise ratio (SNR) of each constituent. In this context, SNR refers to the ratio between estimated constituent amplitude and corresponding estimated amplitude error, which is determined in a "first-pass" analysis via bootstrapping (see Pawlowicz et al. 2002, for details). The final synthesised tidal current prediction output would then be calculated by a "second pass" based on the refined set of constituents. Since

the tidal analysis is carried out independently for each grid point, it would be straightforward to choose a new set of constituents for each grid point.

Nonetheless, for this specific observation dataset, whose quality is highly variable on the grid, we consider as more appropriate to use a fixed set of constituents as for the entire grid in order to avoid confounding changes in the quality of observations with changes in the tidal processes. The selection of constituents to be included was based on an examination of their major axis amplitudes and SNR on the entire grid as well as at a grid point (54.3° N, 8.1° E) which is characterised by high observation coverage over time and low expected GDOP. For example, constituents whose amplitude estimate is very low on the entire grid and for which the spatial pattern appears random were discarded, while those with high amplitudes and/or high SNR on the entire grid or at least at the mentioned grid point with high coverage and low GDOP were retained. The final set of constituents used for the tidal analyses comprises diurnal (O1, K1), semi-diurnal (N2, M2, S2) and higher-frequency components (M4, MS4, M6, 2MS6).

The impact of missing values in the HF radar data on the estimation of tidal parameters and wind correlations discussed in the next section was analysed using numerical model output with synthetic data gaps. For the considered data set, the influence was found to be negligible, and therefore, results for such "synthetic observations" are not shown separately in the following.

2.4 Wind data and correlation analysis

To examine the correlation between surface currents and wind, the complex correlation coefficient ρ (Kundu 1976) between the time series of two-dimensional surface currents at each grid point of the HFR observation grid and a corresponding time series of the two-dimensional wind field was calculated. Two wind time series were initially examined: one based on local measurements at the eastern HFR system location (St. Peter-Ording) and one extracted from the ECMWF data at the grid point closest to the centre of the HFR observation grid (54.5° N, 8.0° E, point C in Fig. 1). In each case, the wind speed U_{10} at 10 m height was considered. The ECMWF wind speed and wind vector direction for the aforementioned grid point for September 1991 is shown in Fig. 5, along with wind magnitude in St. Peter-Ording for comparison. The differences between these two data sources during the period which was further examined (September 1991) are considered to be small. These differences did not result in appreciable changes in the analysis results presented here.

For the surface currents and wind time series, each two-dimensional horizontal vector with zonal component u and meridional component v was converted to a complex vector w defined as

$$w(t) = u(t) + i\,v(t)\,. \tag{1}$$

From each surface current vector w_1 and the common wind vector w_2, a complex correlation coefficient ρ was calculated as

$$\rho(w_1, w_2) = \frac{\langle w_1^* w_2 \rangle}{\langle w_1^* w_1 \rangle^{\frac{1}{2}} \langle w_2^* w_2 \rangle^{\frac{1}{2}}}, \tag{2}$$

where a superscript star (*) denotes the complex conjugate and $\langle \cdot \rangle$ the arithmetic average over time. This definition was adopted from Kundu (1976) who analysed the systematic deviation to the left (cyclonic in the northern hemisphere) of currents in the bottom layer compared to the direction of geostrophic velocities. Kundu (1976) demonstrated that the capabilities of classical approaches to evaluate the veering suffer from strongly varying angles (weak currents events increase the uncertainty in veering angle). The magnitude $|\rho|$ is informative for the strength of correlation while the phase angle $\arg(\rho)$ illustrates the veering angle, which is "meaningful" only if the magnitude of the correlation is high.

In the correlation analysis presented in the following, we use wind and surface current vectors which coincide in time. The decision not to analyse time-lagged correlations, which could account for the response time of drift currents, has been taken after some additional analyses had been carried out. It appeared that accounting for a time lag of 6 h (the temporal resolution of wind data) leads to reduced correlations without substantial change of the horizontal patterns.

3 German Bight circulation

3.1 Horizontal transport

The circulation of the German Bight has been addressed in numerous studies with a major focus on numerical modelling of tides (Flather 1976; Maier-Reimer 1977; Backhaus 1980; Davies and Furnes 1980). Numerical simulations of Carbajal and Pohlmann (2004) had approached the state-of-the-art with high enough horizontal resolution (1.5 min in the north–south and 2.5 min in the east–west direction, which corresponds to approximately 3 km) and realistic forcing needed to adequately address similarity between observations and simulations. Operational forecasting performed at the German Hydrographic Service (BSH) provides high-quality, fine-resolution products online (BSH 2011). Furthermore, the work of Staneva et al. (2009) provided the framework for addressing here the agreement between numerical simulations and HFR observations.

Earlier studies mentioned above and Otto et al. (1990), Dick and Sötje (1990), Dippner (1990), Schrum (1997) and Dick et al. (2001) (see also the references therein) as well as the present numerical simulations show that the wind supports a residual circulation in the direction of propagation of the tidal wave (from west to east along the southern boundary and from south to north along the coasts of Germany and Denmark). Simulations carried out with the numerical model described in Section 2.2 demonstrated that the tidal signal associated with the amphidromy at 55.5° N, 5.5° E travels along the coast of the area shown in Fig. 1 in about 3 to 4 h. Tidal range is from 2.5 m (easternmost and northernmost coastal locations) to about 3.5 m (the Elbe river mouth), which allows the coastal area to be classified as exposed to upper mesotidal conditions.

Figure 7 shows time-averaged surface current, vertically averaged current and vertically integrated transport (vertically averaged current times local depth) for September 1991. This presentation of circulation is needed in order to illustrate the field which we further analyse, that is, the surface current (Fig. 7a), and to give an idea about consistency between surface and vertical mean current or transport in the studied area. The surface current has a pronounced maximum along the southern coast and shows a convergence from west to east. Absolute maxima are located in the regions of straits connecting intertidal basins with the open ocean.

Vertically averaged current (Fig. 7b) reveals some important differences from the surface current, in particular along the western model boundary where the meridional component is much stronger in the vertically averaged current. The dominating zonal surface layer transport in the interior and northern part of the model area is replaced by a northward transport in the pattern of vertically averaged current. In both plots, the region around the island of Helgoland shows a pronounced regional pattern.

Time-mean vertically integrated circulation in most of the German Bight area is cyclonic, which is mainly due to the dominant eastward winds. This type of circulation follows approximately the direction of propagation of the tidal wave. A local minimum of the vertically integrated horizontal transport occurs in the coastal East and North Frisian Wadden Sea.
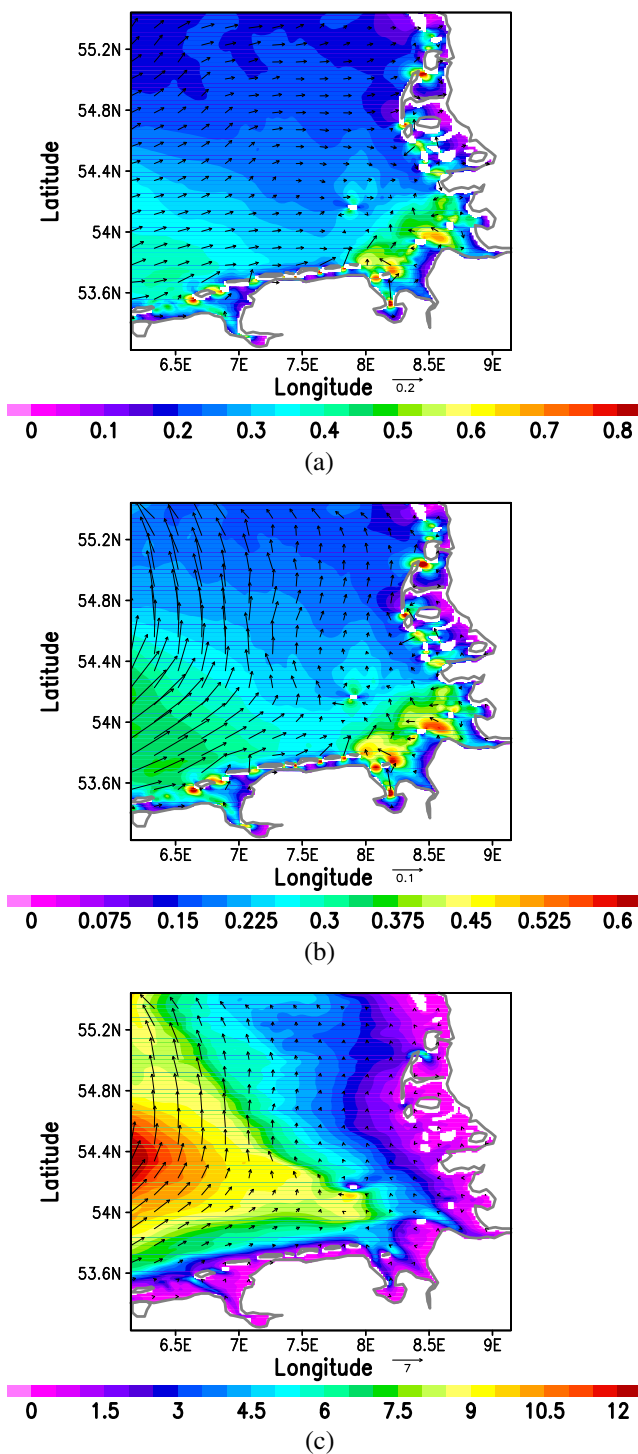
Fig. 7 Time-mean of currents simulated by the German Bight model for September 1991. Current magnitude is color-coded according to the *colorbars*. The *arrow* below each plot corresponds to current or vertically integrated current in metres per second or square metres per second, correspondingly. **a** Surface current, **b** vertical mean current, **c** vertically integrated current

The magnitude of vertically integrated transport displays to a larger extent the characteristics of the German Bight topography, which is dominated by the underwater extension of the Elbe Estuary. The position of the northern bank of this estuary reduces the penetration of open ocean waters into the shallow coastal zone substantially, and consequently, the direction of incoming flow turns abruptly to north–northwest.

3.2 The effect of density

The role of density for the circulation in the German Bight has been addressed by Carbajal and Pohlmann (2004); however, their work focused primarily on the modification of characteristics of tidal ellipses. The study of Czitrom et al. (1988) analysed the applicability of the theory of Simpson and Hunter (1974) to the German Bight area, which is dominated by freshwater fluxes from Elbe and Weser rivers. They considered the parameter $\xi = \log(hu_0^{-3})$, which characterises the intensity of tidal stirring, where h is the water depth and u_0 is the tidal current amplitude. Low values of ξ indicate strong mixing and vice versa. Their study showed that ξ is below the subcritical value of about 2 in large parts of the Wadden Sea. This is an illustration that coastal areas shallower than ≈ 20 m are strongly exposed to tidal mixing. In the southeastern corner of the German Bight, well-mixed areas extend almost up to the island of Helgoland. The lack of in situ measurements of currents in these coastal areas justifies giving further consideration to the role of density using results from numerical modelling validated against HFR observations. This is of utmost importance for the German Bight, which is a typical representative of a region of freshwater influence (ROFI).

In our model area, which is a mix of very shallow coastal areas and depths bigger than the Ekman depth, dynamics are much more complicated than in the theoretical case of Ekman currents. In the shallow part, the surface drift current is supposed to follow wind direction, in the deeper part deflection of surface current from the direction of wind is larger. The expectation is that the correlation between wind and surface currents will replicate topography changes; however, the effect of density is difficult to specify in advance because the joint role of wind and density for the regional circulation is still not clear.

To investigate how density affects the physical forcing in the German Bight, the following two experiments were performed:

– A model run with temperature and salinity variable in time and space. This simulation provides a surface current field $\mathbf{u}_{vd} = (u_{vd}, v_{vd})$ and is referred to as variable density (vd) run in the following.

– A model run with constant temperature and salinity. This simulation provides a surface current field $\mathbf{u}_{cd} = (u_{cd}, v_{cd})$ and is referred to as constant density (cd) run in the following.

By examining the difference between these two experiments, we want to illustrate the role of density and to give a motivation for the analyses provided in the remainder of the paper.

In the following analysis, the total surface current vector $\mathbf{u} = (u, v)$ is decomposed into two components: tidal current $\mathbf{u}^{tides}$ (predicted by a synthesis of analysed tidal constituents) and non-tidal components $\mathbf{u}^{res}$ obtained by subtracting tidal from total current, i.e.

$$\mathbf{u}^{tot} = \mathbf{u}^{res} + \mathbf{u}^{tides} . \tag{3}$$

It is noteworthy that the tidal current component $\mathbf{u}^{tides}$ is different in the two experiments.

We discuss below the correlation between surface current and wind. We focus on the surface current because HF radars measure this property. Assuming a linear dependence between wind stress and 10 m wind would mean that correlation between wind and surface current is proportional to the work done by wind (this work is measured by the variance between wind stress and surface current) normalised by the energy of the transient non-tidal current (this energy is measured by $\langle |\mathbf{u}^{res}|^2 \rangle$). Thus, the comparison between the above mentioned correlations in the two experiments is expected to reveal how density modifies surface forcing.

Patterns of correlation between wind and non-tidal currents (Fig. 8a, b) are qualitatively similar in the two experiments. As it could be expected from general considerations, in the presence of density stratification, the correlation between wind and surface current decreases. This tendency is better seen in the deep part of the basin demonstrating the role of stratification as a factor modifying the relationship between wind and surface current.

An unexpected outcome was the similarity between the two experiments of the correlation between wind and surface current in the areas of river mouths. Both revealed two minima, in front of the Elbe and Weser estuaries, correspondingly. Without the experiment with constant density, one could erroneously attribute the local minima in the correlation pattern to the effect of density in the ROFIs. The local minima observed in the experiment with constant density are not caused by river runoff, and so these local features must result from similar circulation characteristics in the two
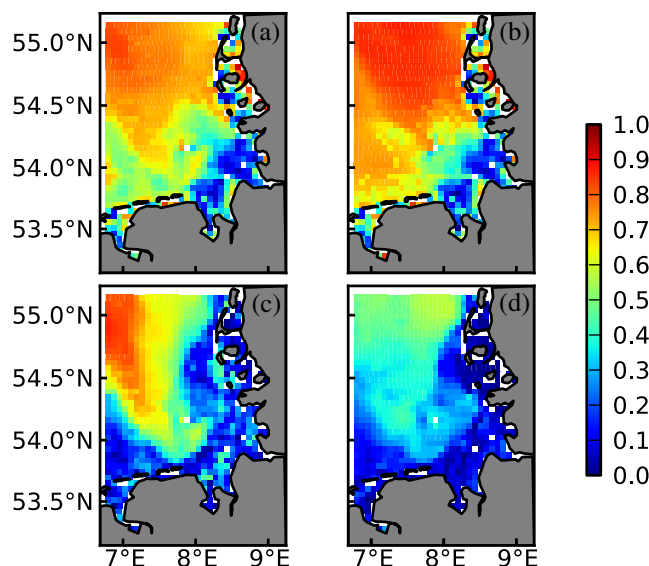
Fig. 8 Magnitude of complex correlation $|\rho|$ of surface velocities with wind. The numerical simulation data is **a** the non-tidal surface velocity in the variable density experiment, **b** the non-tidal surface velocity in the constant density experiment, **c** the difference between the non-tidal velocity in the variable density and constant density experiments and **d** the difference between the total velocity in the variable density and constant density experiments

experiments (recall that the wind forcing is identical in the two experiments). Obviously, complex coastline and bathymetry is the dominating factor shaping the circulation in the same way in the two experiments.

The variance of surface currents in the German Bight provides further insight. In both experiments, this variance reaches the largest magnitude in the southeastern corner of the Bight. In this area, the sea level range has a maximum, the circulation readjusts from eastward (along the southern coast) to northward (along the eastern coast) and the bottom topography also changes and shows small-scale features. All these factors together tend to enhance instability of circulation, thus reducing the correlation between surface current and wind.

Even in the relatively simple case of constant density, one finds some very clear regional characteristics, which need more attention: (1) The area of large correlation between wind and surface current reaches the coast in the area of the North Frisian Wadden Sea, while in the southern part of the model area relatively low correlation is observed far to the north of the East Frisian Wadden Sea. This cannot be explained by the differences in topography along the two coasts because shallow water reaches larger extension in front of the North Frisian Wadden Sea (see Fig. 1). (2) The western open boundary is characterised by smaller

correlations in comparison to the northern one. (3) The small area with lower correlation west of the island of Helgoland coincides with a region in the extension of Elbe Estuary where depths slightly decrease (see Fig. 1). These results demonstrate that in the constant density case, the impact of wind on the circulation is very complex. In this context, we refer to Fig. 1 of Czitrom et al. (1988) where the isoline $\xi = 2.2$ shows a similar configuration (far from the coast in the southern area and approaching Sylt in the North). However, we remind that the patterns addressed by Czitrom et al. (1988) were dominated by the tidal current amplitude, whereas we consider the non-tidal current in our correlation analysis. This result could indicate that the near coastal water is not only well mixed due to strong tidal currents, but also that the non-tidal circulation in these areas is extremely unstable (large variance in surface current tends to reduce correlation with the wind) and perhaps difficult to predict.

Analysis of the difference between variable and constant density runs is presented in the following using the complex correlation between wind and the differential surface current $\mathbf{u}_{diff}^{res} = \mathbf{u}_{cd}^{res} - \mathbf{u}_{vd}^{res}$ in the two experiments $\rho\left(\mathbf{u}_{diff}^{res}, \mathbf{U}_{10}\right)$ (Fig. 8c). The result, which illustrates the role of density in the modification of the forcing of coastal ocean by wind, reveals an increase in the magnitude of the complex correlation in an area around the island of Helgoland, which extends up to the northern model boundary. In the entire shallow coastal zone and in the southwest of the domain $\rho\left(\mathbf{u}_{diff}^{res}, \mathbf{U}_{10}\right)$ is small. We remind here that the result in Fig. 8c does not give the difference between Fig. 8a, b. Rather, it shows that the size and location of the effects of density are expected

to affect the surface forcing by wind. Coupling between wind and surface current is stronger in the deeper area, which is usually characterised by a stronger vertical stratification than shallow and well-mixed coastal area.

Analysis of the differential surface current $\mathbf{u}_{diff}^{res}$) sheds more light on the problem of the impact of density (Fig. 9). Overall, the magnitude of the differential velocity in the central part of the model area is of the order of the time-mean velocity magnitude (compare Fig. 7). Furthermore, change in the direction of currents from the variable density experiment to the one with constant density is such that density tends to deflect surface current in the interior of the model area to the right. On the contrary, in the coastal zone, deflection is in the opposite sense or is very small. As demonstrated by additional analyses of individual velocity components (data not shown here), the above results are mostly due to the differences in meridional velocity. Conclusions here are similar as from the correlation analysis: (1) The impact of baroclinicity is stronger in the interior part of the German Bight and (2) the deflection of surface current has a minimum in the coastal area, as well as in the southwestern part of the German Bight.

From the comparison of correlation patterns of $\rho\left(\mathbf{u}_{diff}^{tot}, \mathbf{U}_{10}\right)$ (Fig. 8d) and the ones of $\rho\left(\mathbf{u}_{diff}^{res}, \mathbf{U}_{10}\right)$ (Fig. 8c), it becomes clear that tidal velocities tend to only decrease the strength of correlation without substantially affecting the correlation pattern. This gives an indication that coupling between tidal current and density is weak.

The wind forcing in some areas addressed here based on the correlation between wind and surface current
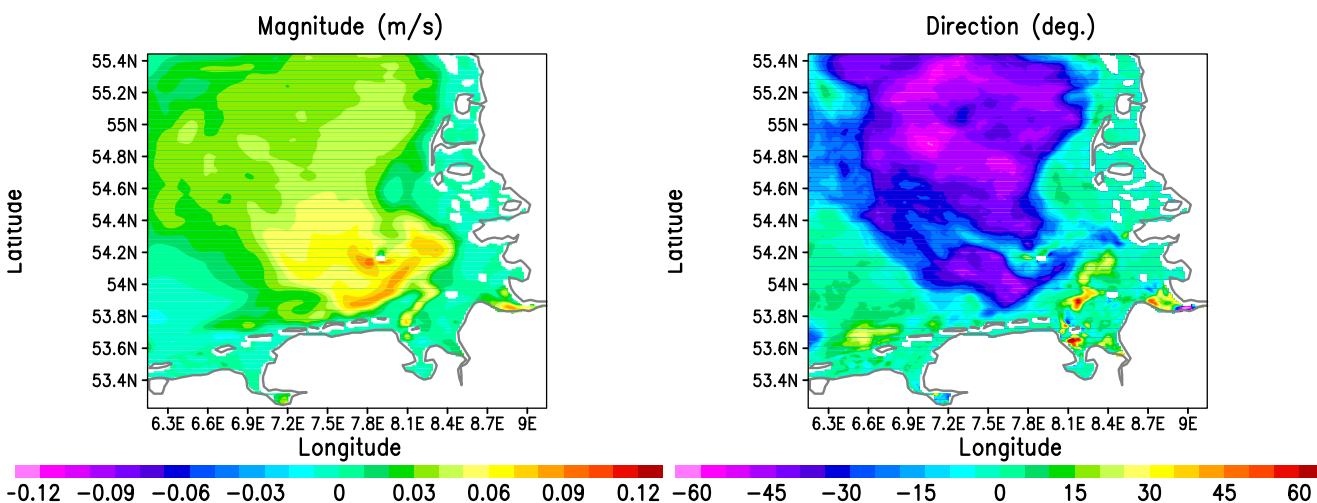
Fig. 9 Difference between time-mean velocity magnitude and direction in two experiments for the month of September 1991 (variable density run minus constant density run), magnitude in metres per second and direction in degrees color-coded according to the *colorbars*

changes dramatically over short distances in both cases "vd" and "cd" experiments. Some of these changes occur in the coastal zone covered by HFR observations presented in Section 2.1. In most of this area, currents are extremely variable, which gives us the motivation to further investigate the consistency between observations and numerical simulations focusing on regional patterns. This could contribute to improving state estimates in this area.

4 Model-data comparison

4.1 Time series

To illustrate the typical characteristics of zonal and meridional surface velocity data from HFR observations in direct comparison with model simulations, several 24-h time series examples are shown in Fig. 10. Velocity components from two locations at 2 days (one
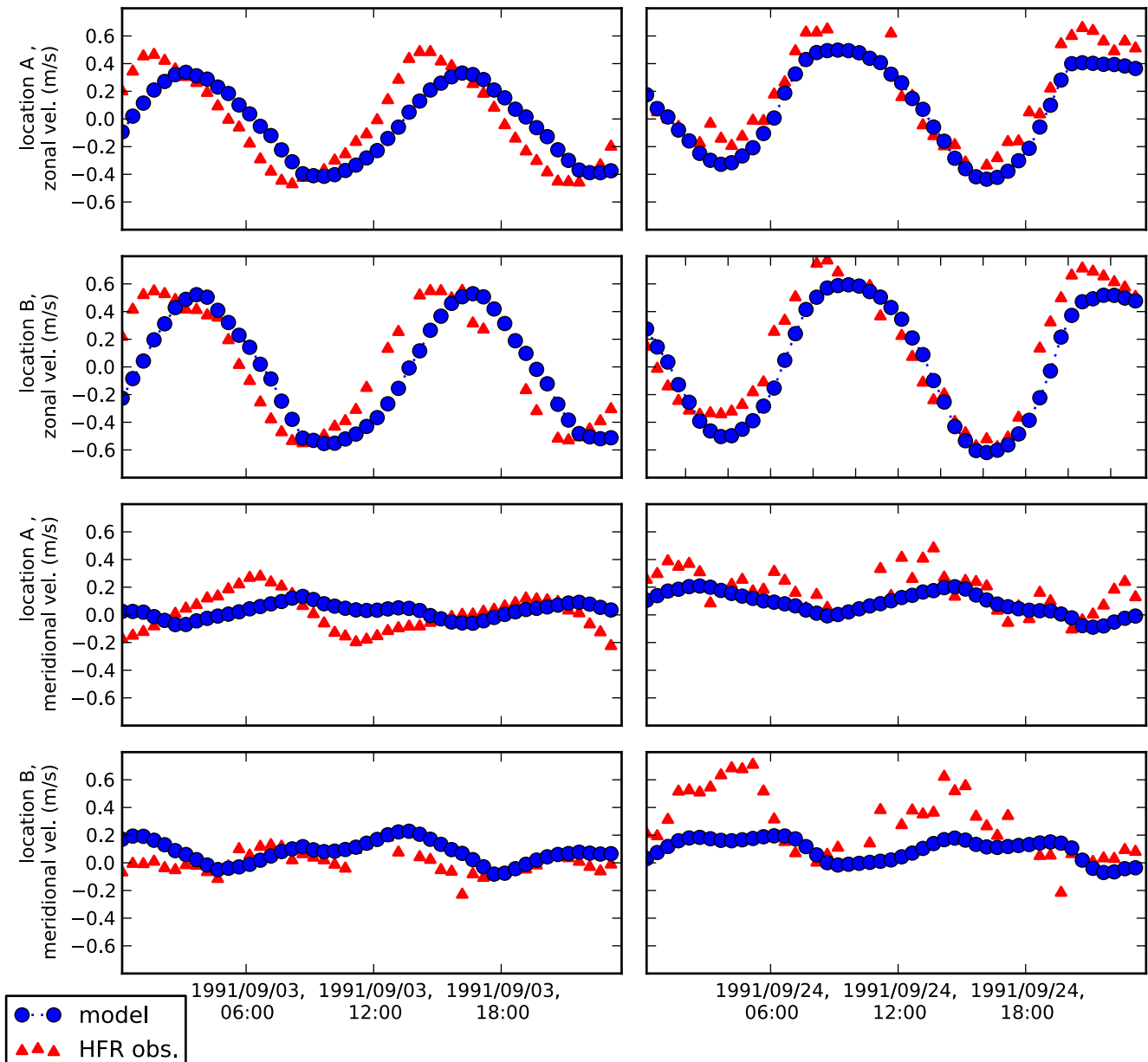
Fig. 10 Time series examples of the zonal and meridional components of the surface velocity (metres per second) for HFR observations (*red triangles*) and model simulations (*blue circles*). From *top* to *bottom*, the panels show zonal velocity at location *A*, zonal velocity at location *B*, meridional velocity at location *A* and meridional velocity at location *B* (see Fig. 2 for location identification). The *left panels* show time series examples for 3 September 1991, a (relatively) calm day, the *right panels* for 24 September 1991, a stormy day (see Fig. 5 for wind data at these times)

relatively calm, the other one relatively stormy) are displayed. Oscillations of zonal velocity are larger than the ones of meridional velocity giving an initial expectation for the zonal elongation of tidal ellipses in the examined area. Obviously, zonal velocity identifies a clear dominance of the M2 signal, which persists both during calm and stormy weather. The temporal variability of meridional component is much less regular and in contrast to the zonal component is dominated by higher than M2 frequencies.

The relatively low level of tidal signal in the meridional velocities explains the relatively large differences between observations and simulations, particularly under stormy weather. The comparison between observations demonstrates that the temporal variability during calm and stormy weather is quite different, which is explained by the large magnitude of the meridional wind component (Fig. 5). Noteworthy is the zonal wind velocity, which is even larger, but does not substantially affect the zonal current, which is strongly dominated by tides.

At location A (see Fig. 1), tidal variability with almost the same characteristics dominates the periods of calm and stormy weather. In contrast, the shapes of the simulated curves in location B, which is to the south of shallows connecting island of Helgoland and the coast, are quite different during the two analysis periods. The same applies to the observation data, however, in a different way. Obviously, any analysis of tidal ellipses will be strongly dependent upon irregular oscillations in the meridional velocity. We remember here that in the previous section these areas were identified by analysis of model data as dominated by large instabilities.

Power spectral density (PSD) estimates for the month of September 1991 confirm the prevalence over time of some of the characteristics visible in the short time series sections. Figure 11 shows the PSD of zonal velocity at location A based on model simulations and HFR observations. This PSD estimate was calculated using Welch's method (Welch 1967) with non-overlapping segments of length 256 samples (linear trend removed) to which a Hanning window (Blackman and Tukey 1959) was applied. The dominant peaks revealing the major tidal periods coincide well both in shape as well as in maximum magnitude between model simulations and HFR observations, always with higher maxima for the latter. At periods in between these distinct peaks and especially for periods around and below 2 h, the HFR observations' PSD remains one to two orders of magnitude above that of the model simulations. This may be attributable to broad spectrum and especially high-frequency noise present in the HFR observations; the latter can already clearly be seen
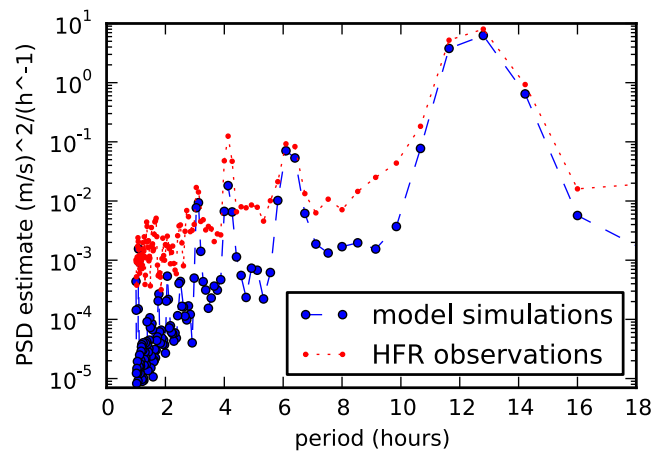

Fig. 11 Power spectral density (*PSD*) estimates of zonal velocity at location A based on model simulations and HFR observations for the month of September 1991

in the short time series sections discussed above. For meridional velocity (data not shown here), similar PSD estimates are obtained, albeit with larger differences in peak magnitudes. This again demonstrates that the local dynamics are quite complex and selectively sensitive to wind, which gives the major motivation to further analyse the local diversity of the sensitivity of circulation to wind forcing in more detail. As a measure of average deviation between numerical simulations and HFR observations over time, the RMS is shown in Fig. 12 for the month of September 1991. Areas of high deviations in the order of 0.2 to 0.3 m/s are visible near the coast at the eastern as well as southeastern edge of the observation grid. Along the line connecting the two radars meridional velocity shows relatively bad agreement (see also Barth et al. 2010). The relatively low values of the RMS deviation (substantially lower than the amplitude of oscillations at least in the zonal direction) gives the motivation for the analysis presented in the following part.

4.2 Tidal constituents and tidal ellipses

For an exemplary grid point (location A, see Fig. 2), amplitudes of tidal constituents from a tidal analysis with 95% confidence intervals (CI) based on numerical simulations as well as HFR observations for September 1991 (Fig. 13) show that for both data sets, a large number of tidal constituents can be distinguished with reasonable confidence and that the patterns of relative amplitudes are quite similar, with the HFR observations almost always leading to higher absolute amplitudes. This exemplary tidal analysis was calculated with all available constituents, while for all further analyses,

Fig. 12 RMS deviation between numerical simulations and HFR observations for the month of September 1991, shown separately for the zonal (*left*) and meridional velocity components (*right*), color-coded according to the *colorbar*
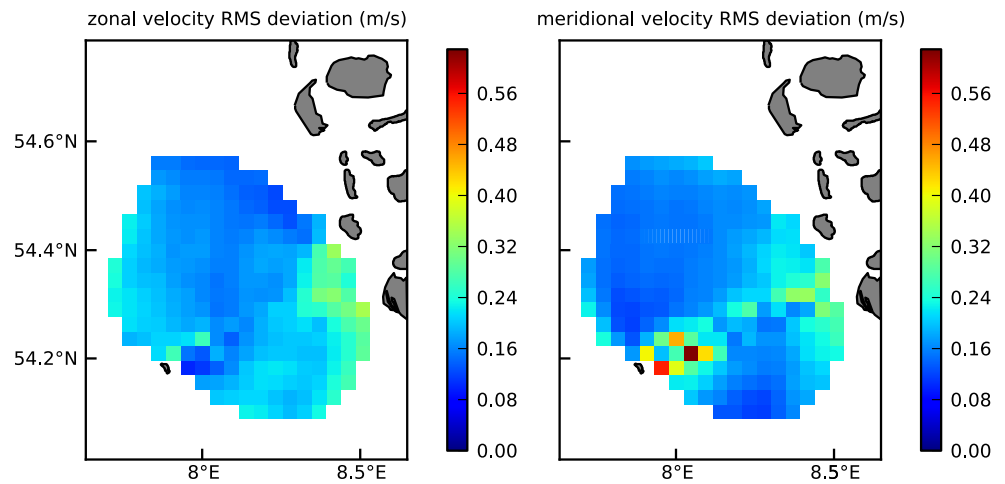
the fixed set of constituents described in Section 2.3 was used.

Tidal ellipses for the M2 constituent calculated from observation and model data for September 1991 are compared in Fig. 14. The mean difference between the semi-major axes based on model simulations compared to those based on HFR observations is 0.07 m/s. For 90% of the observation grid points, the difference is less than 0.14 m/s. The mean relative difference between two estimates is 17%. From north to south, ellipses degenerate to an almost exclusively zonal movement, which is more pronounced in the HFR observations due to a much stronger meridional component of velocity in the northern half of the region of interest. Here,

eccentricity is also systematically lower for the HFR observations, in many areas combined with a shift in orientation away from the zonal towards the meridional axis when compared to the model data. In the southeastern corner of the region (the ROFI of the Elbe), a shift towards a northwest/southeast orientation is visible in both data sources. This trend is more pronounced in the model output. Here, a region of clockwise rotation is also present in both data sources, although with a clearly larger extent in the model data. A smaller region of clockwise rotation northeast of Helgoland is visible only in the model data. Changes of ellipse parameters appear smooth on this spatial scale for both data sources, with slightly more abrupt
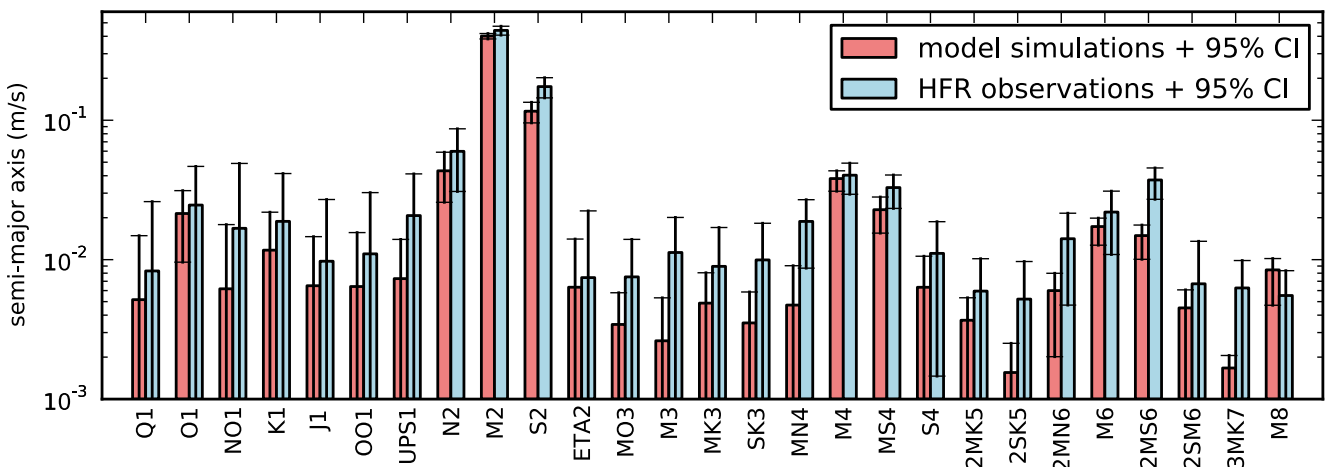
Fig. 13 Tidal constituent amplitudes with 95% CI from a tidal analysis with all available constituents based on model simulations (*red, left bars*) and HFR observations (*blue, right bars*). Note that the log-scale simplifies the comparison of the relative length of CI. Data are taken from an exemplary grid point

(location A, see Fig. 2) for the month September 1991. Tidal constituents are ordered with increasing frequency from *left* to *right*. The ones with a period longer than 30 h and/or semi-major axis less than 0.001 m/s are excluded from the figure for clarity
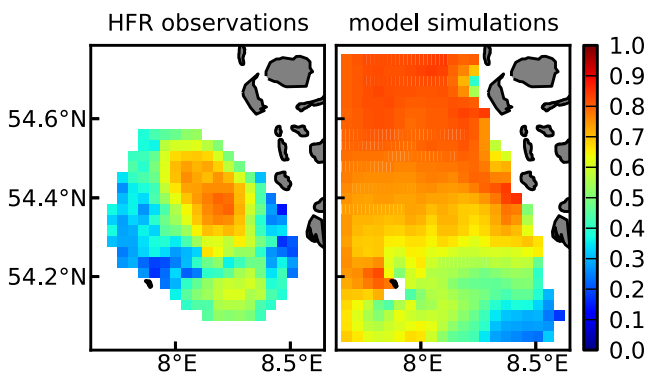
Fig. 14 Dominant tidal
ellipses (M2 frequency)
derived from HFR
observations (*left panel*) and
model simulations (*right
panel*). The sense of rotation
of the ellipses is color-coded,
blue representing
counterclockwise (positive
ellipticity) and *red* clockwise
(negative ellipticity) rotation.
Analysis based on 1 month of
data (September 1991) at
intervals of 30 min (1,440
samples in time for
observation grid points with
full coverage over time)
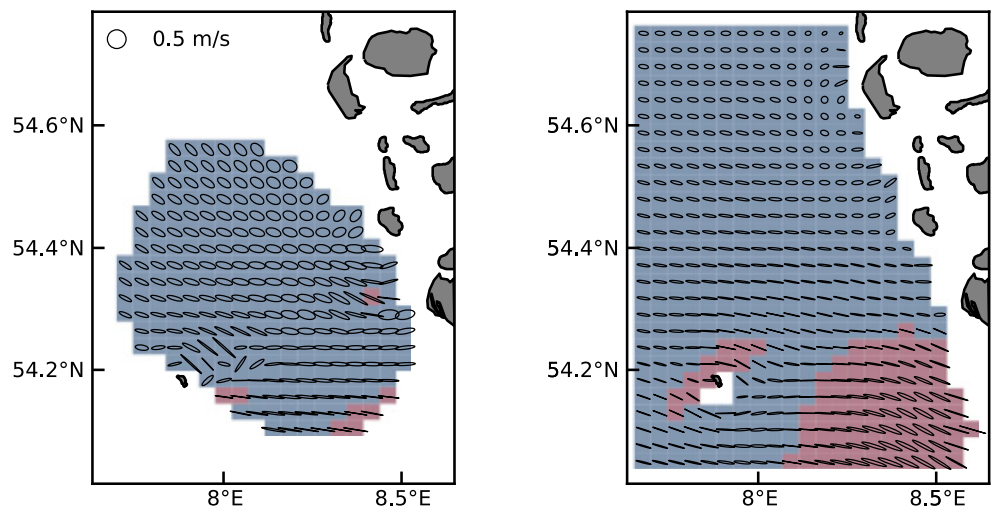
changes revealed by the HFR observations northeast
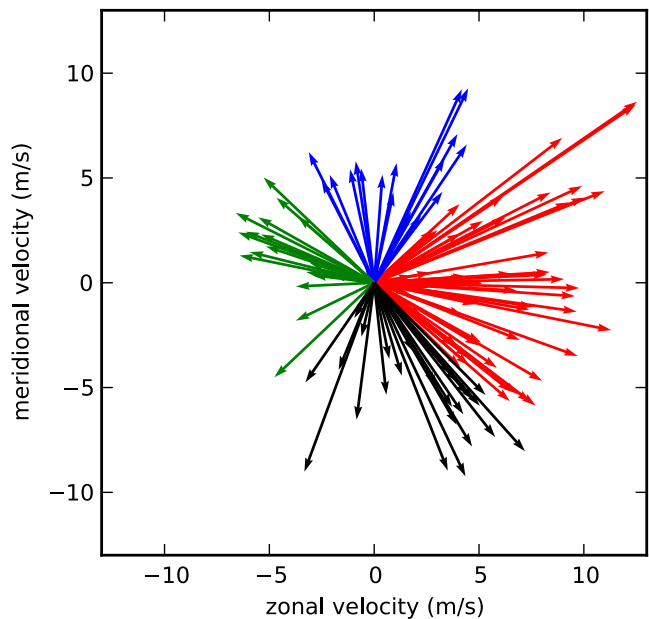of Helgoland as well as west of St. Peter-Ording.

4.3 Patterns of correlation with wind

The magnitude of complex correlation $|\rho|$ of surface
currents with ECMWF winds for the month of Sep-
tember 1991 is shown in Fig. 15 based on HFR ob-
servations as well as model output. For the model
data, the prominent structure is a meridional gradient
in the correlation pattern. For the HFR observations,
although a similar gradient seems present, it is overlaid
by decreasing correlation magnitude at all edges of the
observation grid as well as near the HFR system loca-
tions. It is plausible that the former could be attributed
to data availability and quality (see Figs. 2 and 4), the
latter to GDOP (see Fig. 3).

As should be expected from general considerations,
as well as from the comparison with Fig. 8a, for HFR
observations, consistently lower values are obtained
when calculating $|\rho|$ based on total currents and even
lower values when based on a tidal current prediction
as provided by the tidal analysis (data not shown here).
To analyse how stable results are depending on the
location of wind data used in the analysis, calculation is
repeated for ρ between wind and HFR total currents in
location 54.0° N, 8.0° E instead of 54.5° N, 8.0° E, that is,
one grid point further south. This change did not result

Fig. 15 Magnitude of complex correlation $|\rho|$ of non-tidal cur-
rents of HFR observations (*left*) and model simulations (*right*)
versus ECMWF wind data. Only data for the month of Septem-
ber 1991 was analysed, leading to a maximum possible number of
samples per grid point of 120 (six-hourly wind data)

Fig. 16 Wind vectors (ECMWF) for September 1991, split into
four bins based on direction: eastward (*red*), northward (*blue*),
westward (*green*) and southward (*black*)
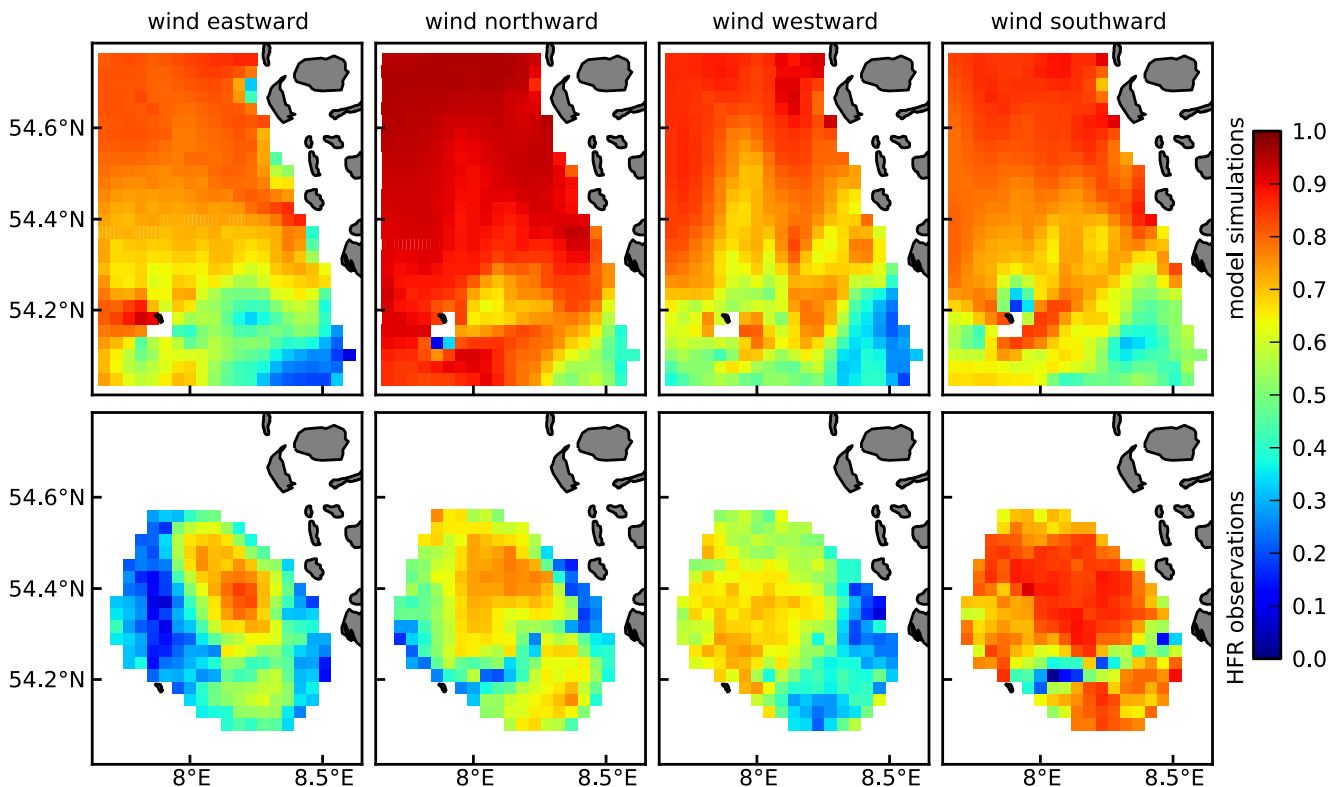
Fig. 17 Magnitude of complex correlation $|\rho|$ exemplified for different wind directions. Based on non-tidal currents from model simulations (*top row*) and HFR observations (*bottom row*), all samples in time were separated into four bins according to the wind direction (see Fig. 16). All correlations were calculated versus ECMWF wind data. Only data for the month of September 1991 was analysed

in appreciable differences in patterns of magnitude or phase angle (data not shown).

For the non-tidal currents, the calculation of $|\rho|$ was repeated for four subsets of the time series, selected based on the wind direction. The four subsets of corresponding wind vectors are shown in Fig. 16, while the resulting maps of $|\rho|$ based on model simulations as well as HFR observations are shown in Fig. 17.

The highest similarity to the corresponding map in Fig. 15 can be found in the subset of eastward wind (we remind that this is the dominant wind direction supporting a cyclonic circulation in German Bight), paired by high magnitudes of the corresponding wind vectors as seen in Fig. 16. Higher values of $|\rho|$ for the subset of northward wind visible in the model simulation data are not visible in the HFR observation data. The prominent contrast between higher values north of the baseline connecting the two HFR systems and lower values south and southeast is visible in almost all subsets. A notable exception is the subset of southward wind of the HFR observations, where high values are also visible south of the baseline.

The presented coherence maps are affected by estimation errors, which are dependent on the available

sample size (eastward 57, northward 18, westward 19, southward 26). The corresponding variance of the estimated coherence magnitude is given by Jacovitti and Cusani (1992):

$$\text{var}(|\rho|) = \frac{1}{2}\frac{1}{N}(1 - |\hat\rho|^2)\,(2 - |\hat\rho|^2) \le \frac{1}{N}\quad, \tag{4}$$

where $\hat\rho$ is the true coherence and N is the number of samples. In the worst case (northward), we get 0.24 as an upper limit of the estimation error standard deviation for each spatial bin. The dominating large-scale patterns found in Fig. 17 clearly stand out of this uncertainty regime and are thus considered as significant.

5 Discussion

5.1 Observations

When examining HFR surface current observations, the highly non-random patterns in time and space of (a) missing values as well as (b) the magnitude of observation error estimates pose challenges for different

types of subsequent analyses. For example, missing data may often be caused by radio frequency interference. For a nearby site (70 km further north) and similar operating frequencies (25 and 30 MHz), Essen et al. (1983) reported a recurring reduction in HFR range by up to a factor of two. This reduction follows the daily cycle of the ionosphere, which causes problems to the analysis of other daily variations, e.g. in the wind field.

HFR observation error estimates include measurement errors and variability within the coherent integration time, as well as a fixed GDOP based on the radar installation geometry. Due to GDOP, the expected dominant spatial pattern in a setup with two HFR system locations is relatively simple, with a rough approximation of one symmetry axis along the baseline and another along a line perpendicular to it and intersecting in the middle between the two HFR systems. Additionally, the error in the surface current measurement increases with distance from the antennas because of a decreasing signal-to-noise-ratio. These idealized patterns are visible in the data examined here, but clearly overlaid with patterns which depend on factors other than the geometric setup on an idealized horizontal plane. The interaction between these factors cannot easily be predicted, and therefore, comparisons with results from a numerical model are very instructive.

5.2 Intercomparison study, geophysical relevance and perspectives

The phase lag between numerical simulations and observations has been demonstrated previously. In a recent study, Barth et al. (2010) showed that optimizing the tidal boundary values via non-sequential assimilation of HFR observations may alleviate this problem to a substantial degree. Higher short-term variance in the HFR observations as well as regular occurrence of higher absolute velocities remain an issue for analyses as well as assimilation purposes.

Deeper analyses on consistencies between HFR observations and numerical simulations, also using recent observations collected in the framework of COSYNA Project (Schulz-Stellenfleth et al. 2010), confirmed the conclusions provided above that as it concerns phase properties of simulations, there is still a room for improvement in the model. Because this issue will be addressed in a forthcoming publication, we will give in the following only some brief information about the source of the identified problem: (1) It appeared that phase differences are also present when we use boundary conditions from other available sources and (2) it appeared that these differences change with neap-spring cycle, getting lower values by high water. At

present it seems that solving this problem would need improving bathymetry of the model.

In the region of HFR observations, good agreement is illustrated between amplitudes of major tidal constituents derived from numerical model and observations. Furthermore, a qualitative agreement can also be found between M2 tidal ellipses based on model simulations and HFR observations, with an overall trend of the ellipses degenerating going from north to south. The differences between HFR observations and model simulations seem to be of a similar magnitude as found in other studies in the German Bight (for example Carbajal and Pohlmann 2004, based on CODAR observations south of Helgoland).

The baseline connecting the two HFRs lies close to a stretch of shallow water known as "Steingrund" (between the island of Helgoland and the mainland coast east of it), which may play a role in separating these distinct subregions. In the model simulations, a region of negative ellipticity in the direction of the Elbe estuary extends almost northward up to Steingrund and is even more pronounced than in the HFR observations. Possible signals from freshwater influence from the Elbe estuary are difficult to ascertain in these observations (let alone compare with nearby estuaries like Weser or Ems) due to the limited extension of the observation grid. This influence may be examined in future studies of data from ongoing HFR installations, again in comparison with model scenarios. To elucidate possible causes for the phase lag in model simulations (for example, inadequate parameterization of bottom friction), independent simultaneous observations of the vertical velocity profiles in addition to HFR surface current observations are highly desirable. One possibility would be a simultaneous ADCP deployment (an approach followed by Davies et al. 2001; Liu et al. 2010, among others).

As mentioned above, another significant source of error in the model simulations is uncertainties of the bathymetry. In the presence of extremely strong mechanical forcing (tides and wind waves), it is not only hydrodynamics which are difficult to measure and simulate but also the morphodynamical response which in turn is expected to impact circulation.

6 Conclusions

The analysis of HFR observations from the "PRISMA" project (PRISMA 1994) presented here is the first extended presentation of this dataset in a refereed journal. The focus here was on the consistency of PRISMA data with model hindcasts from a model setup which is

currently used in pre-operational coastal ocean applications (Schulz-Stellenfleth et al. 2010).

Because inconsistency is considered as an inherent property of observational systems and numerical models, we focused here not only on the geophysical relevance of observations and results from simulations but also on their limits and problems. This was motivated by our interest to objectively estimate the state of coastal ocean and associated errors. Overall consistency was found in terms of zonal and meridional components of velocity time series, ellipse parameters of the dominant M2 tidal constituent as well as small-scale spatial patterns of the magnitude of complex correlation of wind and surface current. This correlation, however, is quite different for different wind directions, proving that the southeast corner of the German Bight exhibits complex dynamics where especially the meridional velocity component is difficult to simulate accurately (see also Barth et al. 2010). This should motivate dedicated studies on the forecasts in the near coastal zone with error estimates.

The agreement between observations and numerical simulations gives credibility to sensitivity analyses carried out with the aim to quantify the contribution of different forcing mechanisms to regional dynamics. We demonstrated that the change of the correlation patterns between wind and surface current from the coastal to open ocean are not only due to density. The effect of coastline and topography are quite pronounced as well.

The complex correlation with a wind vector time series shows a pattern somewhat similar to the degenerating M2 tidal ellipses, with the magnitude of correlation decreasing in the southeast direction towards the Elbe estuary. This overall pattern can generally be found in both model simulations as well as HFR observations. Even when comparing only grid points where the observation coverage over time is at least 50%, effects of the GDOP as well as decreasing coverage towards the edge and baseline are likely and hinder a clear interpretation. Even under a dominant tidal forcing, as can be found in the German Bight, wind effects may be substantial, in particular if longer time scales are concerned. Intra-annual variability is highly probable and demands further examination based on time series of appropriate length, either from historical datasets or ongoing installations.

We demonstrated that HFR observations resolve well small-scale and rapidly evolving characteristics of coastal currents. As such, they could present an important component to observational platforms in the German Bight with a good spatial and temporal discretisation and good accuracy. In parallel research (Schulz-Stellenfleth et al. 2010), as well as in Barth et al. (2011) and Schulz-Stellenfleth and Stanev (2010), it is demonstrated that HFR surface current observations could substantially improve estimates on physical state and consequently increase the predictive capabilities of numerical models, ultimately providing an important component for regional operational oceanography.

References

Backhaus JO (1980) Simulation von Bewegungsvorgängen in der Deutschen Bucht. Dtsch Hydrogr Z 15:7–56

Barrick DE, Evans MW, Weber BL (1977) Ocean surface currents mapped by radar. Science 198(4313):138–144

Barth A, Alvera-Azcárate A, Weisberg RH (2008) Assimilation of high-frequency radar currents in a nested model of the West Florida Shelf. J Geophys Res 113(C8). doi:10.1029/2007JC004585

Barth A, Alvera-Azcárate A, Gurgel KW, Staneva J, Port A, Beckers JM, Stanev E (2010) Ensemble smoother for optimizing tidal boundary conditions by assimilation of high-frequency radar surface currents. Application to the German Bight. Ocean Sci 6:161–178

Barth A, Alvera-Azcárate A, Beckers JM, Staneva J, Stanev EV, Schulz-Stellenfleth J (2011) Correcting surface winds by assimilating high-frequency radar surface currents in the German Bight. Ocean Dyn. doi:10.1007/s10236-010-0369-0

Blackman RB, Tukey J (1959) Particular pairs of windows. In: The measurement of power spectra, from the point of view of communications engineering. Dover, New York

Breivik Ø, Sætra Ø (2001) Real time assimilation of HF radar currents into a coastal ocean model. J Mar Syst 28(3–4):161–182. doi:10.1016/S0924-7963(01)00002-1

BSH (2011) Berechnete strömungen des operationellen modellsystems des BSH. http://www.bsh.de/aktdat/modell/stroemungen/Modell1.htm

Burchard H, Bolding K (2002) GETM—a general estuarine transport model. Tech. rep., Institute for Environment and Sustainability, ISPRA, Italy

Carbajal N, Pohlmann T (2004) Comparison between measured and calculated tidal ellipses in the German Bight. Ocean Dyn 54(5):520–530

Chapman RD, Shay LK, Graber HC, Edson JB, Karachintsev A, Trump CL, Ross DB (1997) On the accuracy of HF radar surface current measurements: intercomparisons with ship-based sensors. J Geophys Res 102(C8):18737–18748

Czitrom S, Budéus G, Krause G (1988) A tidal mixing front in an area influenced by land runoff. Cont Shelf Res 8(3):225–237

Davies AM, Furnes GK (1980) Observed and computed M2 tidal currents in the North Sea. J Phys Oceanogr 10(2):237–257

Davies AM, Hall P, Howarth MJ, Knight PJ, Player RJ (2001) Comparison of observed (HF radar and ADCP measurements) and computed tides in the North Channel of the Irish Sea. J Phys Oceanogr 31(7):1764–1785

Dick S, Eckard K, Müller-Navarra S, Klein H, Komo H (2001) The operational circulation model of BSH (BSHcmod)—model description and validation. Berichte des Bundesamtes für Seeschifffahrt und Hydrographie (BSH) 29, BSH

Dick SK, Sötje K (1990) Ein operationelles Ölausbreitungsmodell für die deutsche bucht. Dtsch Hydrogr Z Ergänzungsheft (A) 16:243–254

Dippner JW (1990) A frontal-resolving model for the German Bight. Cont Shelf Res 13:49–66

Essen HH, Gurgel KW, Schirmer F (1983) Tidal and wind-driven parts of surface currents, as measured by radar. Ocean Dyn 36(3):81–96

Essen HH, Gurgel KW, Schlick T (2000) On the accuracy of current measurements by means of HF radar. IEEE J Oceanic Eng 25(4):472–480. doi:10.1109/48.895354

Flather RA (1976) A tidal model of the north-west European continental shelf. Mem Soc R Sci Liège, ser 6 10:141–164

Graber HC, Haus BK, Chapman RD, Shay LK (1997) HF radar comparisons with moored estimates of current speed and direction: expected differences and implications. J Geophys Res 102(C8):18749–18766. doi:10.1029/97JC01190

Gurgel KW, Antonischki G, Essen HH, Schlick T (1999a) Wellen Radar (WERA): a new ground-wave HF radar for ocean remote sensing. Coast Eng 37:219–234. doi:10.1016/S0378-3839(99)00027-7

Gurgel KW, Essen HH, Kingsley SP (1999b) HF radars: physical limitations and recent developments. Coast Eng 37:201–218

Hoteit I, Cornuelle B, Kim S, Forget G, Köhl A, Terrill E (2009) Assessing 4D-VAR for dynamical mapping of coastal high-frequency radar in San Diego. Dynam Atmos Ocean 48(1–3):175–197. doi:10.1016/j.dynatmoce.2008.11.005

Jacovitti G, Cusani R (1992) Performance of normalized correlation estimators for complex processes. IEEE Trans Signal Process 40(1):114–128. doi:10.1109/78.157187

Janssen F, Schrum C, Backhaus J (1999) A climatological data set of temperature and salinity for the Baltic Sea and the North Sea. Ocean Dyn 51(0):5–245

Kundu PK (1976) Ekman veering observed near the ocean bottom. J Phys Oceanogr 6(2):238–242

Lipa B, Nyden B, Ullman DS, Terrill E (2006) SeaSonde radial velocities: derivation and internal consistency. IEEE Ocean Eng Soc Newsl 31(4):850–861. doi:10.1109/JOE.2006.886104

Liu Y, Weisberg RH, Shay LK (2007) Current patterns on the West Florida Shelf from joint self-organizing map analyses of HF radar and ADCP data. J Atmos Ocean Technol 24(4):702–712. doi:10.1175/JTECH1999.1

Liu Y, Weisberg RH, Merz CR, Lichtenwalner S, Kirkpatrick GJ (2010) HF radar performance in a low-energy environment: CODAR SeaSonde experience on the West Florida Shelf. J Atmos Ocean Technol 27(10):1689–1710, doi:10.1175/2010JTECHO720.1

Maier-Reimer E (1977) Residual circulation in the North Sea due to the M2 tide and mean annual wind stress. Ocean Dyn 30(3):69–80

Otto L, Zimmerman JTF, Furnes GK, Mork M, Saertre R, Becker G (1990) Review of the physical oceanography of the north sea. Neth J Sea Res 26:161–238

Paduan JD, Shulman I (2004) HF radar data assimilation in the Monterey Bay area. J Geophys Res 109(C7). doi:10.1029/2003JC001949

Parks AB, Shay LK, Johns WE, Martinez-Pedraja J, Gurgel KW (2009) HF radar observations of small-scale surface current variability in the Straits of Florida. J Geophys Res 114(C8). doi:10.1029/2008JC005025

Pawlowicz R, Beardsley B, Lentz S (2002) Classical tidal harmonic analysis including error estimates in MATLAB using t_tide. Comput Geosci 28(8):929–937

PRISMA (1994) Prozesse im Schadstoffkreislauf Meer-Atmosphäre: Ökosystem Deutsche Bucht. BMFT-Projekt 03F0558A1 (1.1.1990–31.10.1993). Abschlussbericht, ZMK-Universität Hamburg

Schirmer F, Essen HH, Gurgel KW, Schlick T, Hessner K (1994) Local variability of surface currents based on HF-radar measurements. In: Sündermann J (ed) Circulation and contaminant fluxes in the North Sea. Springer, Berlin

Schrum C (1997) Thermohaline stratification and instabilities at tidal mixing fronts. Results of an eddy resolving model for the German Bight. Cont Shelf Res 17(6):689–716

Schulz-Stellenfleth J, Stanev E (2010) Statistical assessment of ocean observing networks—a study of water level measurements in the German Bight. Ocean Model 33(3–4):270–282

Schulz-Stellenfleth J, Wahle K, Staneva J, Seemann J, Cysewski M, Gurgel K, Schlick T, Ziemer F, Stanev E (2010) Nutzung eines HF-Radarsystems zur Beobachtung und Vorhersage von Strömungen in der Deutschen Bucht im Rahmen von COSYNA. DGM Nachrichten 3/10:3–8

Shulman I, Paduan JD (2009) Assimilation of HF radar-derived radials and total currents in the Monterey Bay area. Deep Sea Res II 56(3–5):149–160. doi:10.1016/j.dsr2.2008.08.004

Simpson J, Hunter J (1974) Fronts in the Irish Sea. Nature 250:404–406. doi:10.1038/250404a0

Soulsby R (1983) The bottom boundary layer of shelf seas. In: Johns B (ed) Physical oceanography of coastal and shelf seas, vol 35, chap 5. Elsevier, Amsterdam, pp 189–266

Staneva J, Stanev E, Wolff JO, Badewien T, Reuter R, Flemming B, Bartholomä A, Bolding K (2009) Hydrodynamics and sediment dynamics in the German Bight. A focus on observations and numerical modelling in the East Frisian Wadden Sea. Cont Shelf Res 29:302–319

Taylor GI (1922) Tidal oscillations in gulfs and rectangular basins. Proc Lond Math Soc s2–20(1):148–181. doi:10.1112/plms/s2-20.1.148

Welch P (1967) The use of fast Fourier transform for the estimation of power spectra: a method based on time averaging over short, modified periodograms. IEEE Trans Audio Electroacoust 15. doi:10.1109/TAU.1967.1161901